

OPEN

Study of solidification pathway of a MoSiBTiC alloy by optical thermal analysis and *in-situ* observation with electromagnetic levitation

Hiroyuki Fukuyama^{1*}, Ryogo Sawada¹, Haruki Nakashima¹, Makoto Ohtsuka¹ & Kyoosuke Yoshimi²

MoSiBTiC alloys are promising candidates for next-generation ultrahigh-temperature materials. However, the phase diagram of these alloys has been unknown. We have developed an ultrahigh-temperature thermal analyser based on blackbody radiation that can be used to analyse the melting and solidification of the alloy 67.5Mo–5Si–10B–8.75Ti–8.75C (mol%). Furthermore, electromagnetic levitation (EML) was used for *in-situ* observation of solidification and microstructural study of the alloy. On the basis of the results, the following solidification pathway is proposed: Mo solid solution (Mo_{ss}) begins to crystallize out as a primary phase at 1955 °C (2228 K) from a liquid state, which is followed by a ($\text{Mo}_{ss} + \text{TiC}$) eutectic reaction starting at 1900 °C (2173 K). Molybdenum boride (Mo_2B) phase precipitates from the liquid after the eutectic reaction; however, the Mo_2B phase may react with the remaining liquid to form Mo_{ss} and Mo_5SiB_2 (T_2) as solidification proceeds. In addition, T_2 also precipitates as a single phase from the liquid. The remaining liquid reaches the ($\text{Mo}_{ss} + \text{T}_2 + \text{TiC}$) ternary eutectic point at 1880 °C (2153 K), and the ($\text{Mo}_{ss} + \text{T}_2 + \text{Mo}_2\text{C}$) eutectic reaction finally occurs at 1720 °C (1993 K). This completes the solidification of the MoSiBTiC alloy.

Casting is very important for heat-resistant metallic materials such as creep-resistant steels and Ni-based superalloys. This is because they contain many solute elements that strengthen them, and preventing their segregation during solidification ensures their microstructural homogeneity and longer stability at operation temperature. Because improving heat resistance of creep-resistance steels and Ni-based superalloys improves heat engine efficiency, developing a casting process using phase diagrams is essential for controlling their solidification.

MoSiB-based alloys are promising candidates for next-generation ultrahigh-temperature materials because of their excellent high-temperature strength^{1–9}. However, it has been difficult to use them in practical applications because their densities are higher than those of Ni-based superalloys¹⁰ and their room-temperature fracture toughness is poor^{3,11–14}. Recently, Yoshimi *et al.* discovered the major advantage of adding TiC to Mo-Si-B alloys produced by casting^{10,15}. The resultant alloys have densities reduced to less than 9 g/cm³, excellent high-temperature strength¹⁶, and good room-temperature toughness¹⁷. Their cast microstructures are basically composed of Mo solid solution (Mo_{ss}), D8_r-structured Mo_5SiB_2 (T_2) and NaCl-type (Ti, Mo)C plus a small amount of $\text{MoC}_{0.5}$ -type orthorhombic (Mo, Ti)₂C¹⁸ depending on composition. It was previously reported^{10,15} that the microstructures are formed through several solidification steps involving three-phase and/or four-phase eutectic reactions. However, the phase diagram of the MoSiBTiC alloy is still unknown.

The phase diagram of the Mo-Si-B ternary system was first constructed by Nowotny *et al.*¹⁹ in the late 1950s. Almost 40 years later, Nunes *et al.*²⁰ reconsidered the liquidus projection for the Mo-rich portion of the Mo-Si-B ternary system on the basis of arc-cast alloy microstructures characterised by scanning electron microscopy (SEM), transmission electron microscopy (TEM) and X-ray diffraction (XRD). Katrych *et al.*²¹ identified the solidification routes, a liquidus projection and a few vertical sections of the ternary phase diagram via differential thermal analysis (DTA), SEM and electron probe microanalysis (EPMA). Yang and Chang²² calculated the phase stability, liquidus projection and solidification paths using thermodynamic modelling. Ha *et al.*²³ modified the

¹Institute of Multidisciplinary Research for Advanced Materials, Tohoku University, Sendai, 980-8577, Japan.

²Department of Materials Science, Graduate School of Engineering, Tohoku University, Sendai, 980-8579, Japan.

*email: hiroyuki.fukuyama.b6@tohoku.ac.jp

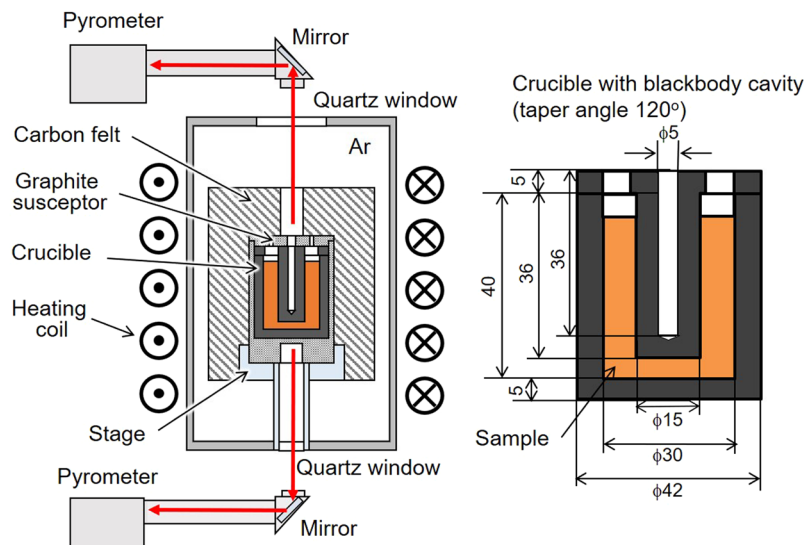


Figure 1. Left: schematic of the ultra-high-temperature thermal-analysis apparatus; Right: crucible with a blackbody cavity.

primary phase regions in the liquidus projection for the Mo-rich portion using SEM and TEM results. Thus, combining thermal and microstructural analyses is essential to establishing phase diagrams.

However, conventional DTA or differential scanning calorimetry (DSC) is insufficient for studying the phase diagram of a MoSiBTiC alloy because of its more complicated solidification steps and technical problems caused by ultrahigh temperature ($>1900\text{ }^{\circ}\text{C}$). Platinum, usually used as a container and thermocouple material, has a too low melting point ($1768\text{ }^{\circ}\text{C}$) to be used for thermal analysis of MoSiBTiC alloys. In addition, uncertainty in temperature measurement becomes significant at ultrahigh temperatures owing to a lack of well-defined fixed-temperature points.

To overcome these experimental difficulties, we have developed a method for ultrahigh-temperature thermal analysis of MoSiBTiC alloys using blackbody radiation. This involves using a radiation pyrometer to measure blackbody radiation emitted from a sample holder having a blackbody cavity. The radiation pyrometer is calibrated at $1950\text{ }^{\circ}\text{C}$ using the eutectic temperature of the Ru-C system. We use the method to thermally analyse one of the alloys to study the reaction temperatures during its solidification process. Although differential thermal analysers can be operated above $2000\text{ }^{\circ}\text{C}$ using a commercially available W-Re thermocouple, the thermocouple will suffer from drift owing to aging and contamination. The advantage of the new method is in the higher accuracy of the temperature measurement and the larger sample volume, which allows for the detection of smaller heat effects.

The thermal analysis requires a way to relate reaction heat peaks to corresponding microstructure formation to reveal the solidification pathway of the MoSiBTiC alloy. Here, we use EML to *in-situ* observe its solidification. We developed an EML technique coupled with a static magnetic field in our previous work^{24–28}. This technique enables high-precision, non-contact thermophysical measurements of high-temperature melts. In this work, we use the technique to *in-situ* observe the solidification of the MoSiBTiC melt, and study the microstructure obtained from a quenched sample of the EML experiment. Finally, the solidification of the alloy is discussed in light of the thermal analysis and *in-situ* observation.

Principle of Ultrahigh-Temperature Thermal Analysis

Figure 1 is a schematic of our ultrahigh-temperature thermal analysis apparatus. This apparatus consists of a radio-frequency furnace, two pyrometers and a crucible having a blackbody cavity. A sample is filled into the crucible and heated through a graphite susceptor by applying a radio-frequency current to the heating coil. The radiation from the blackbody cavity is observed with a pyrometer at the top of the apparatus through a quartz glass and a mirror, measuring the sample temperature T_s . The susceptor temperature T_c is monitored with a pyrometer at the bottom of the apparatus, which is used for temperature control. The temperature determination of the sample is based on the Planck equation

$$E_b = \frac{C_1}{\lambda^5 \left\{ \exp\left(\frac{C_2}{\lambda T}\right) - 1 \right\}}, \quad (1)$$

where E_b is the emissive blackbody power, λ is the wavelength, T is the absolute temperature, and C_1 and C_2 are the first and second radiation constants equal to $3.7415 \times 10^{-16}\text{ W}\cdot\text{m}^2$ and $1.4388 \times 10^{-2}\text{ m}\cdot\text{K}$, respectively. The emissivity ε_c of the blackbody cavity is expressed in terms of the emissivity ε_m of the crucible material and aspect ratio α of the cavity²⁹:

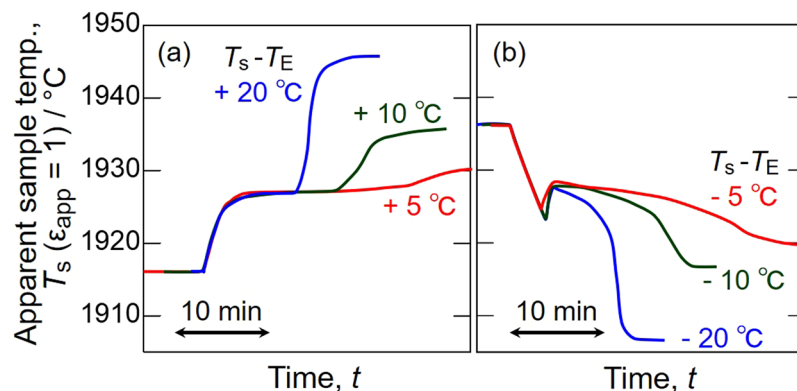


Figure 2. Apparent temperature curves of Ru-C alloy on (a) heating and (b) cooling.

$$\varepsilon_c = 1 - \frac{(1 - \varepsilon_m)\pi}{\alpha^2} \quad (2)$$

The value of ε_c was calculated as 0.999 for graphite with the aspect ratio of the blackbody cavity (diameter of 5 mm; depth of 36 mm). The emissive power of the blackbody cavity, E_c , is

$$E_c = \tau\varepsilon_c E_b = \varepsilon_{app} E_b, \quad (3)$$

where τ is the absorptivity of the quartz glass and mirror, and ε_{app} is the apparent emissivity. From Eqs (1) and (3), the absolute temperature is expressed using the emissive power of the blackbody cavity, E_c :

$$T = \frac{C_2}{\lambda \left\{ \ln \left(\frac{\varepsilon_{app} C_1}{E_c \lambda^5} + 1 \right) \right\}} \quad (4)$$

In this study, ε_{app} was obtained using fixed-temperature points. The highest fixed-temperature point defined by the international temperature scale (ITS-90) is the melting point T_m of Cu (1084.62 °C)³⁰. Yamada *et al.*³¹ have proposed eutectic temperatures (T_E) of metal-carbon binary systems for fixed-temperature points above T_m for Cu. Because the liquidus temperature of MoSiBTiC alloys seems to be higher than 1900 °C, T_E values for Ru-C (1953 °C³¹) and Ni-C (1329 °C³¹) alloys were chosen as the fixed points in addition to T_m for Cu. We considered the effect of eutectic reaction kinetics on measuring fixed points on the basis of the Fe-C eutectic transition temperature reported by Sasajima *et al.*³²

Results

Ultrahigh-temperature thermal analysis. *Fixed-temperature points.* The ultrahigh-temperature analyser was calibrated with the melting point of pure Cu and the eutectic temperatures of the Ru-C and Ni-C alloys. As an example, Fig. 2 shows the apparent temperature curves of the Ru-C eutectic alloy obtained upon heating and cooling assuming $\varepsilon_{app} = 1$. The sample temperature was initially set lower than T_E by 10 °C and kept there for thermal homogenisation. The sample was heated again to a temperature higher than T_E by 5, 10 and 20 °C until the eutectic plateau was completed as shown in Fig. 2(a). After the eutectic melting plateau was completed, the sample was cooled to a temperature lower than T_E by 5, 10 and 20 °C to obtain the eutectic plateau on cooling (Fig. 2(b)). In Fig. 2(a), the duration of the eutectic plateau on heating decreases, meaning the eutectic reaction rate increases, with increasing set temperature. However, the eutectic temperature does not change with reaction rate. The cooling curves in Fig. 2(b) show that the eutectic temperature after undercooling slightly depends on set temperature. This difference is understood in terms of eutectic solidification kinetics. Thus, the eutectic plateau obtained on heating was used as the fixed point in this study, and its average apparent T_E for the Ru-C alloy was 1928 °C. By substituting the apparent T_E and $\varepsilon_{app} = 1$ into Eq. (4), E_c was obtained for the Ru-C alloy, and E_b was estimated via Eq. (1) for the true T_E of the Ru-C alloy (1953 °C). Similar measurements were conducted to obtain T_E for the Ni-C alloy and T_m for Cu. Figure 3 shows a linear relationship between E_b and E_c for these fixed-temperature points. The apparent emissivity ε_{app} was determined to be 0.945 from the slope. From these results, the uncertainty in temperature measurements for the thermal analysis was evaluated as $\pm 0.4\%$ within a temperature range from 1084.62 to 1953 °C.

MoSiBTiC alloy. The composition of the MoSiBTiC alloy used in this study was 67.5Mo-5Si-10B-8.75Ti-8.75C (mol%). The alloy was thermally analysed using the above method with $\varepsilon_{app} = 0.945$. Heating and cooling steps were repeated three times. Figure 4 shows a typical cooling curve of the MoSiBTiC alloy obtained in the second cooling step. Five inflection points appear on the cooling curve. Table 1 shows the temperatures of all inflection points and their averages for three cooling curves. Reactions corresponding to the inflection points will be discussed later.

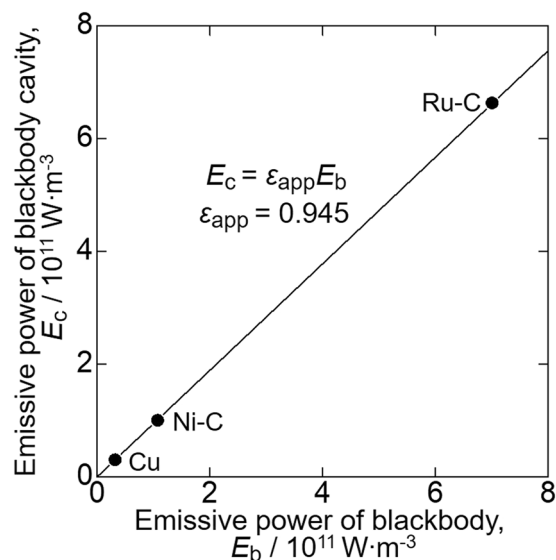


Figure 3. Relationship between E_b and E_c at T_m for Cu and T_E for Ni-C and Ru-C alloys.

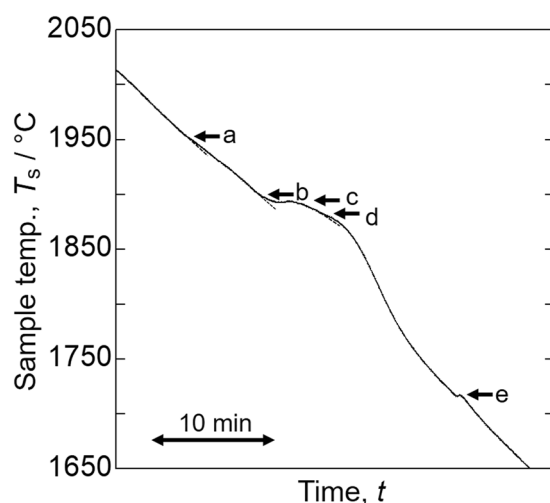


Figure 4. Cooling curve of the MoSiBTiC alloy.

Inflection points	1 st (°C)	2 nd (°C)	3 rd (°C)	Average (°C)
A	1950	1954	1962	1955 (2228 K)
B	1899	1903	1899	1900 (2173 K)
C	1894	1894	1894	1894 (2167 K)
D	—	1881	1879	1880 (2153 K)
E	1719	1717	1725	1720 (1993 K)

Table 1. Inflection point temperatures of MoSiBTiC alloy (67.5Mo–5Si–10B–8.75Ti–8.75C in mol%).

Solidification behavior of MoSiBTiC melt obtained by EML. *Multiple recalescence.* The MoSiBTiC alloy was levitated and melted using EML in a static magnetic field to observe the solidification of the melt. Figure 5 (top) shows the cooling temperature profile of the MoSiBTiC alloy melt after the heating laser was turned off. We recorded multiple light emissions from the alloy melt owing to the release of latent heat (recalescence), and these emissions were assigned to peaks A–E on the temperature profile from the *in-situ* CCD camera observation. An example is the bottom of Fig. 5, which is a sequential top-view image of the alloy melt around recalescence D, at which the melt surface became brighter. Consequently, solidification of the melt started with recalescence A and finished with recalescence E. Here, the sample temperature was measured using a pyrometer calibrated with the liquidus temperature (1955 °C) of the alloy as determined in the preceding section. However,

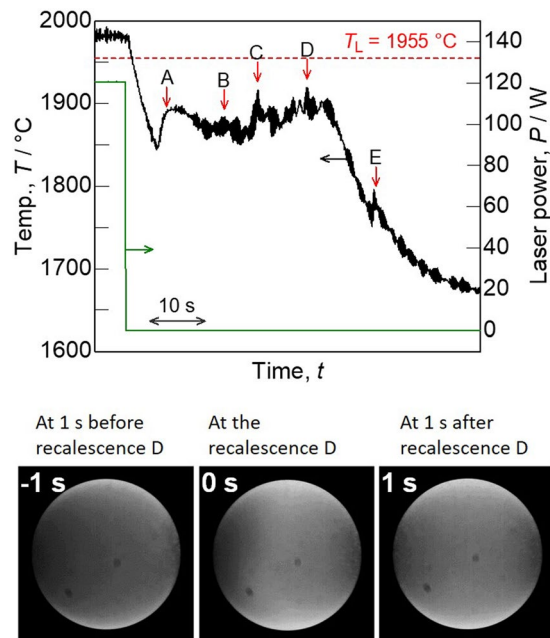


Figure 5. Top: temperature profile of the MoSiBTiC alloy melt levitated via EML on cooling. Multiple recalescences (A–E) were recorded. Bottom: sequential top-view image of the alloy melt shows light emission caused by recalescence D.

after recalescence, the sample temperature was affected by solids precipitated on the melt surface because the partially solidified portion had a different emissivity from that of the melt. For this reason, the recalescence points A–E correspond to the inflection points a–e in Fig. 4, but the recalescence temperatures do not agree with the inflection points.

Solidification microstructural analysis. The levitated MoSiBTiC alloy melt was rapidly solidified from recalescence in EML to freeze the microstructure at that temperature. For microstructural analysis, the partially solidified alloys were held at these temperatures for 10 min just after recalescences B and D as shown in Fig. 6(a,b), respectively, to develop the microstructures. This was followed by the rapid solidification under a He gas flow. This figure also shows partial temperature profiles during the rapid cooling with an enlarged time scale, and top-view images of the partially solidified alloys during the holding time. Solid precipitated from the alloy melt is seen in the laser spot at the centre. Liquid and solid phases are distinguished by their emissivity difference on the alloy surface.

Figure 7(a,b) show the XRD profiles of the quenched samples obtained via the EML experiments of Fig. 6(a,b), respectively. The diffraction peaks of molybdenum solid solution (Mo_{ss}) were clearly observed, and Mo_5SiB_2 (T_2), TiC, Mo_2C and Mo_2B phases were also identified in the quenched samples.

Figure 8(a,b) show the cross-sectional SEM images of the quenched samples obtained via the EML experiments of Fig. 6(a,b), respectively. Phase identification was performed with SEM energy-dispersive X-ray spectrometry (SEM-EDX) considering the XRD results. As shown in Fig. 8(a), the microstructure has large Mo_{ss} grains (white), which should be primarily crystallized in the alloy melt. A TiC (black) phase is seen in the ($\text{Mo}_{\text{ss}} + \text{TiC}$) binary-eutectic structure, as are some minor phases: Mo_2B (light grey), T_2 (grey) and Mo_2C (dark grey). Furthermore, fine ($\text{Mo}_{\text{ss}} + T_2 + \text{TiC}$) and ($\text{Mo}_{\text{ss}} + T_2 + \text{Mo}_2\text{C}$) ternary-eutectic structures are observed. In the microstructure in Fig. 8(b), Mo_{ss} and T_2 phases and ($\text{Mo}_{\text{ss}} + \text{TiC}$) binary-eutectic structure are seen. The ($\text{Mo}_{\text{ss}} + T_2 + \text{TiC}$) ternary-eutectic structure is more developed than the structure in Fig. 8(a). A fine ($\text{Mo}_{\text{ss}} + T_2 + \text{Mo}_2\text{C}$) ternary-eutectic structure is also observed.

Discussion

Solidification pathway. We discuss the solidification pathway of the MoSiBTiC alloy (67.5Mo–5Si–10B–8.75Ti–8.75C in mol%) in light of the thermal analysis and EML experiments. The results are as follows:

1. Five inflection points (a–e) were detected on the cooling curve in Fig. 4.
2. Five recalescences (A–E) were *in-situ* observed as shown in Fig. 5.
3. Mo_{ss} , Mo_2B and T_2 single phases, one binary-eutectic structure ($\text{Mo}_{\text{ss}} + \text{TiC}$) and two ternary-eutectic structures ($\text{Mo}_{\text{ss}} + T_2 + \text{TiC}$) and ($\text{Mo}_{\text{ss}} + T_2 + \text{Mo}_2\text{C}$) were observed in the microstructures of Fig. 8(a,b).

From the above results, we propose the solidification pathway for the MoSiBTiC alloy in Table 2. Inflection points a–e in Fig. 4 correspond to recalescences A–E in Fig. 5, respectively. We note again that, except for the liquidus temperature, the recalescence temperatures in Fig. 5 do not agree with the inflection points of Fig. 4

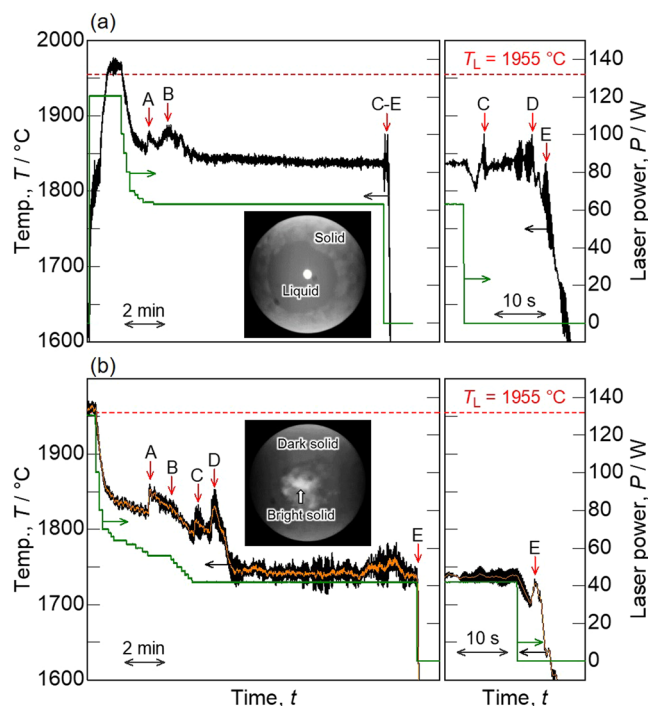


Figure 6. Temperature profile of the MoSiBTiC alloy melt levitated via EML on cooling. (a) The alloy was held for 10 min at the temperature after recalescence B, and (b) the alloy was held for 10 min after recalescence D. Partial temperature profiles with an enlarged time scale are also added to show peaks during the rapid cooling. The inserts in both figures are top-view images of the partially solidified alloy during the holding time.

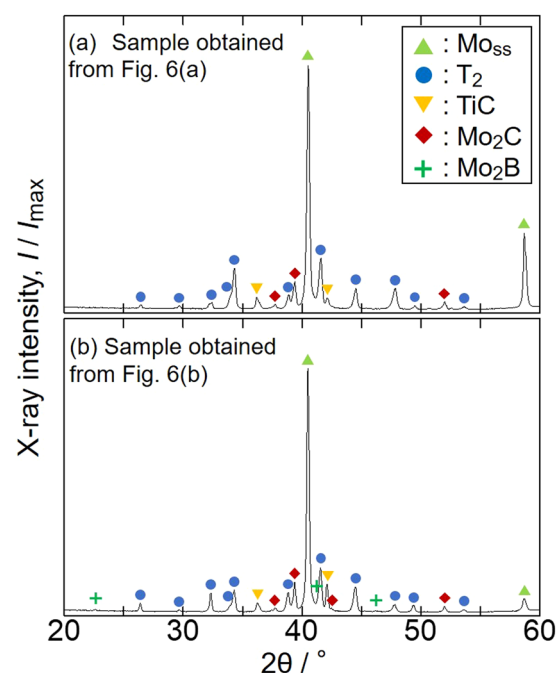


Figure 7. XRD profiles of the rapidly solidified MoSiBTiC alloys obtained from the experiments of Fig. 6(a,b).

because the emissivity of the MoSiBTiC alloy melt levitated by EML was altered by solids crystallized on the melt surface during cooling.

Effect of undercooling on the solidification pathway. Deep undercooling may affect the solidification pathway of alloy melts. For example, Lü and Wang^{33,34} reported that the transition of the primary phase crystallization to the non-equilibrium peritectic phase crystallization is dependent on the degree of undercooling of the melt. In

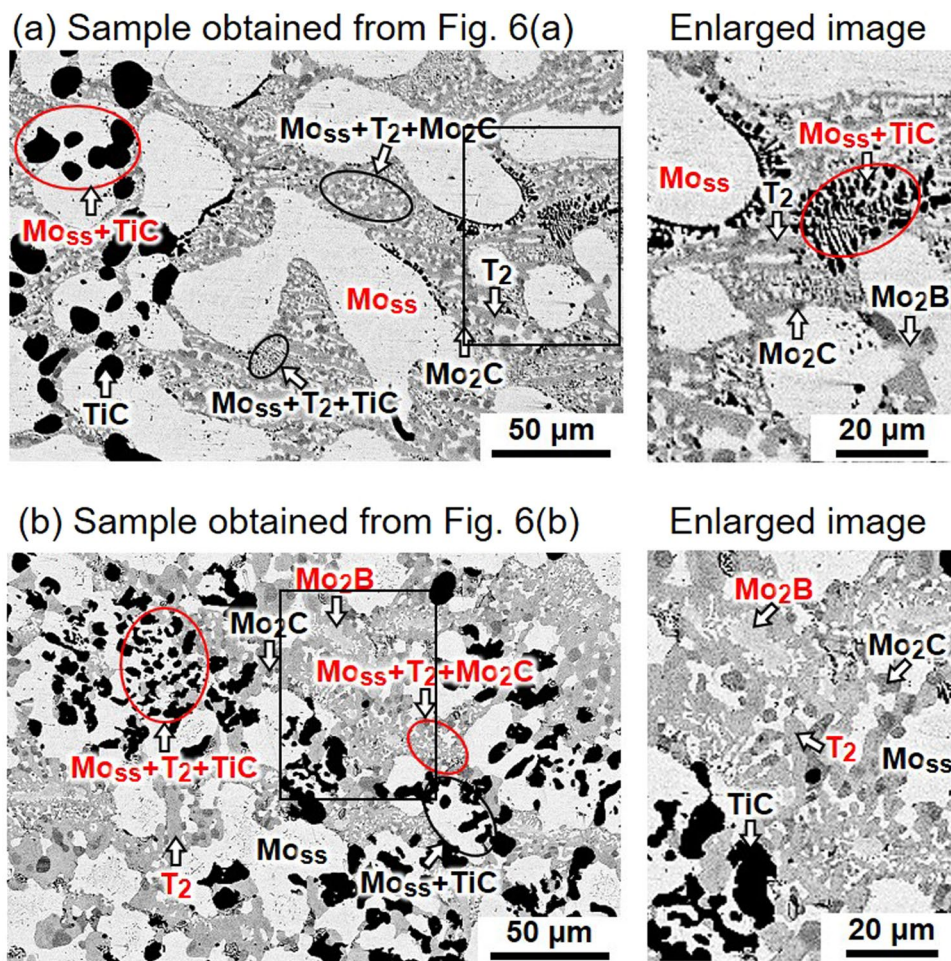


Figure 8. Cross-sectional SEM images of rapidly solidified MoSiBTiC alloys obtained from the experiments of Fig. 6(a,b).

Inflection point obtained in Fig. 4	Recalescence appeared in Fig. 5	Reactions occurred at the inflection temperature
a: 1955°C (2228 K)	A	Liq. → Mo _{ss} primary
b: 1900°C (2173 K)	B	Liq. → Mo _{ss} + TiC (eutectic)
c: 1894°C (2167 K)	C	Liq. → Mo ₂ B Liq. + Mo ₂ B → Mo _{ss} + T ₂
d: 1880°C (2153 K)	D	Liq. → T ₂ Liq. → Mo _{ss} + T ₂ + TiC (eutectic)
e: 1720°C (1993 K)	E	Liq. → Mo _{ss} + T ₂ + Mo ₂ C (eutectic)

Table 2. Solidification pathway of MoSiBTiC alloy (67.5Mo–5Si–10B–8.75Ti–8.75C in mol%).

the present study, the undercooling of the MoSiBTiC alloy melt reached 100–130 °C as shown in Figs 5 and 6. After the first undercooling, recalescence A occurred but the sample temperature did not increase to the initial liquidus temperature. This does not imply a metastable phase formation, but was simply caused by the liquidus composition shift toward the boundary line between Mo_{ss} and TiC primary phases during recalescence A and the subsequent (Mo_{ss} + TiC) binary-eutectic reaction. Therefore, the sample temperature rise was lowered from the initial liquidus temperature and was limited to the (Mo_{ss} + TiC) binary-eutectic temperature (1900 °C). This is understood by the microstructural observation. The microstructures shown in Fig. 8 indicate that the large Mo_{ss} grains were primarily crystallized in the alloy melt, which was followed by the (Mo_{ss} + TiC) binary-eutectic reaction. Thus, the undercooling did not affect the solidification pathway in the present study.

Discussion based on the Mo-Si-B-TiC phase diagram. The chemical composition of the MoSiBTiC alloy (67.5Mo–5Si–10B–8.75Ti–8.75C in mol%) we used is located on the Mo-Si-B-TiC quaternary phase diagram in Fig. 9(a). The alloy composition is also expressed as 75.6Mo–8.9Mo₅SiB₂ (T₂)–15.6TiC in mol% in the

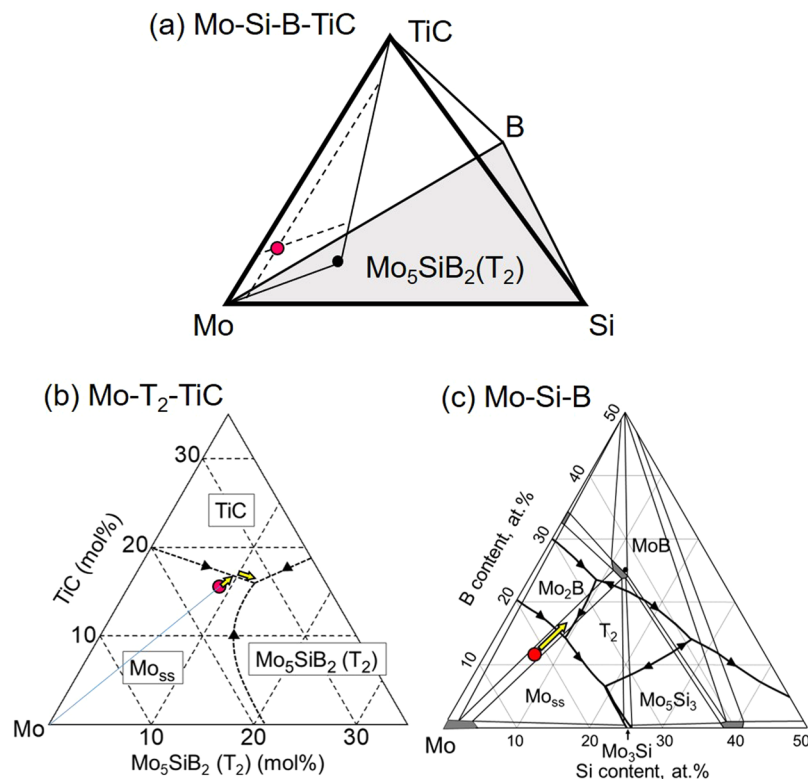


Figure 9. (a) Mo-Si-B-TiC quaternary phase diagram, (b) Mo-Mo₅SiB₂(T₂)-TiC ternary phase diagram and (c) Mo-Si-B ternary phase diagram²³.

Mo-T₂-TiC ternary system, and is plotted in Fig. 9(b). In this ternary system, the alloy composition is initially located in the Mo_{ss} primary phase region. Therefore, after the Mo_{ss} primary phase precipitates at 1955 °C (inflection point a), the liquid composition shifts toward the Mo_{ss}/TiC boundary lines, then the binary eutectic reaction



occurs at 1900 °C (inflection point b) in Fig. 9(b). Eremenko and Velikanova³⁵ reported a eutectic temperature of 2175 °C for the Mo-TiC binary system. Here, the reaction (5) occurred at 1900 °C in the Mo-Si-B-TiC system.

However, the alloy composition is projected onto the basal plane (the Mo-Si-B ternary system) as shown in Fig. 9(c)²³. The initial alloy composition exists in the Mo_{ss} primary phase region on the connecting line between Mo and Mo₅SiB₂(T₂). However, Mo_{ss} content in the liquid is decreased by the eutectic reaction (5), and therefore, the liquid composition moves into the Mo₂B primary phase region as shown in Fig. 9(c). However, this Mo₂B phase soon reacts with the liquid to form Mo_{ss} and T₂ via the reaction



Nunes *et al.*³⁶ reported that this reaction occurs in the four-phase equilibrium at about 2100 °C in the Mo-Si-B ternary system. In our study, the reaction (6) occurred at 1894 °C (inflection point c) in the Mo-Si-B-TiC system.

Going back to the Mo-T₂-TiC ternary phase diagram (Fig. 9(b)), the liquid reaches the ternary eutectic point after the eutectic reaction (5), then the following reaction occurs at 1880 °C (inflection point d):



In addition, the elongated shape of the T₂ grains in Fig. 8(b) indicates that the T₂ phase precipitated out as a single phase from the liquid phase between reactions (6) and (7).

Finally, the (Mo_{ss} + T₂ + Mo₂C) eutectic reaction occurred at 1720 °C (inflection point e), which does not appear on the Mo-Si-B-TiC phase diagram. The order of the two ternary eutectic reactions (6) and (7) is judged from the relatively well-developed (Mo_{ss} + T₂ + TiC) eutectic structure compared with the (Mo_{ss} + T₂ + Mo₂C) eutectic structure. Thus, the solidification is complete.

Miyamoto *et al.*¹⁰ reported the solidification pathway of a similar MoSiBTiC alloy designated as B₂ (70.0Mo-3.3Si-6.7B-10.0Ti-10.0C in mol%): Mo_{ss} (primary) → (Mo_{ss} + TiC) eutectic → T₂ → (Mo_{ss} + T₂ + TiC) eutectic → (Mo_{ss} + T₂ + Mo₂C) eutectic. This process was proposed on the basis of microstructures of as-cast alloy from arc melting and heat-treated alloy at 1800 °C for 24 h. It is difficult to figure out the full solidification process only from microstructural observation. Here, our proposed solidification pathway based on the combination of thermal analysis, *in-situ* observation and EML quenching supports the results obtained by Miyamoto *et al.*

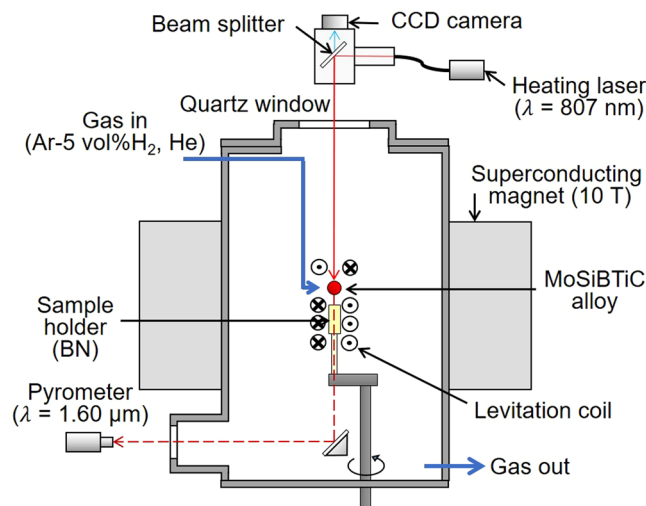


Figure 10. Schematic of the EML apparatus.

In summary, a method for ultra-high-temperature thermal analysis was developed. The maximum measurement error was 5 °C with a temperature range from 1084.62 to 1953 °C. By using this technique, the MoSiBTiC alloy (67.5Mo–5Si–10B–8.75Ti–8.75C in mol%) was thermally analysed. EML experiments were also conducted to observe the *in-situ* solidification of the MoSiBTiC alloy melt, and to study the microstructure of the rapidly solidified sample. The solidification pathway was finally proposed as given in Table 2.

Methods

Ultra-high-temperature thermal analysis. *Fixed-temperature points.* The raw materials for the Ru–C alloy were Ru (99.9 mass%; particle diameter < 500 μm; JX Nippon Mining & Metals, Japan) and C (99.99 mass%; particle diameter < 10 μm; Kojundo Chemical Laboratory, Japan) powders. Ru–C mixed powder with a composition of Ru–11 mol% C was filled into a graphite crucible having a blackbody cavity with a tape angle of 120°, and then heated and cooled in a radio-frequency furnace under an Ar atmosphere at an Ar flow rate of 10 mL/min. The apparent sample temperature T_s was determined assuming $\varepsilon_{app} = 1$ with a top pyrometer measuring the radiation from the blackbody cavity. Initially the Ru–C sample was kept at $T_s = T_E - 10^\circ\text{C}$ to stabilise the furnace temperature, after which it was heated to $T_s = T_E + (5, 10, 20)^\circ\text{C}$ at a rate of 5 °C/min. After the sample was kept at $T_s = T_E + 10^\circ\text{C}$, it was cooled to $T_s = T_E - (5, 10, 20)^\circ\text{C}$ at a rate of 5 °C/min. This procedure was used for other fixed-point measurements with T_m for Cu and T_E for Ni–C. A Cu rod (99.99 mass%; diameter of 2 mm; length of 2 mm; Kojundo Chemical Laboratory, Japan) and Ni rod (99.99 mass%; diameter of 2 mm; length of 2 mm; Rare Metallic, Japan) were used as raw materials. The Ni–C alloy was prepared with the composition Ni–4 mol% C. The apparent emissivity ε_{app} of the pyrometer was determined in advance using T_m for Cu and T_E for the Ni–C and Ru–C alloys.

MoSiBTiC alloy. The MoSiBTiC alloy was prepared by arc-melting from Mo (99.99 mass%; diameter of 10 mm; length of 300 mm; A.L.M.T.), Si (99.999 mass%; particle size of 2–5 mm; Kojundo Chemical Laboratory, Japan), B (99.5 mass%; particle size of 3–7 mm; Kojundo Chemical Laboratory, Japan) and TiC (99 mass%; particle size of 2–5 μm; Kojundo Chemical Laboratory, Japan) as raw materials. The chemical composition of the alloy was 67.5Mo–5Si–10B–8.75Ti–8.75C (mol%). Here, T_2 is a ternary compound (Mo_5SiB_2). A CaO-stabilised ZrO_2 crucible having a blackbody cavity was used to hold the MoSiBTiC alloy (about 87 g) instead of a graphite crucible to prevent carbon contamination. The alloy was heated and cooled in a radio-frequency furnace under an Ar atmosphere at an Ar flow rate of 10 mL/min. The sample was heated at a rate of 10 °C/min and kept around 2000 °C for 30 min to ensure homogeneous melt, and subsequently cooled at a rate of 10 °C/min. The sample temperature was determined during heating and cooling with a top pyrometer measuring the radiation from the blackbody cavity. The inflection points on the cooling curves were treated as the phase transformation temperatures of the MoSiBTiC alloy.

EML experiments on the MoSiBTiC alloy. The schematic of the EML apparatus is shown in Fig. 10. After the MoSiBTiC sample was placed on the sample holder made of BN, the chamber was evacuated to 10^{-2} Pa using a rotary pump and a turbomolecular pump. The chamber was filled with Ar–5 vol% H_2 gas after evacuation. Alternating electric current was applied to the levitation coil to levitate and heat the sample. The sample was melted with a heating laser (wavelength of 807 nm; power of 8–140 W; Jenoptik Laserdiode, Japan; NBT-S140mkII), and the sample temperature was controlled with the laser power. Ar–5 vol% H_2 gas was supplied at a rate of 3 L/min to prevent sample oxidation. A static magnetic field of 10 T was applied to the sample droplet to suppress both its translational motion and convection. For *in-situ* observation of solidification, the sample droplet was filmed with a CCD camera (MC1310; MIKROTRON GmbH, Germany) with a resolution of 512×512 pixels at 60 fps. The sample temperature was measured using a single-colour pyrometer (temperature range of 450–2500 °C; spectral range of 1.45–1.8 μm; IGA140/MB25; IMPAC Pyrometers; LumaSense

Technologies, Germany), which was calibrated at the liquidus temperature of the MoSiBTiC alloy. The sample was held at the temperature right after recalescence for 10 min to grow crystallized grains. After holding each temperature, the heating laser was turned off and He gas was blown at a rate of 5 L/min to quench the sample. SEM (JEOL; JCM-5700) and XRD (Bruker; D2 Phaser) were used to observe and analyse microstructures in a cross-section of the solidified sample.

Received: 29 June 2019; Accepted: 16 September 2019;

Published online: 21 October 2019

References

- Akinc, M. *et al.* Bron-doped molybdenum silicides for structural applications. *Mater. Sci. Eng. A* **261**, 16–23 (1999).
- Yoshimi, K. *et al.* Yielding and flow behavior of Mo₅Si₃ single crystals. *Scripta Mater.* **45**, 1321–1326 (2001).
- Schneibel, J. H., Kramer, M. J., Ünal, Ö. & Wright, R. N. Processing and mechanical properties of a molybdenum silicide with the composition Mo-12Si-8.5B (at.%). *Intermetallics* **9**, 25–31 (2001).
- Dimiduk, D. M. & Perepezko, J. H. Mo-Si-B alloys: developing a revolutionary turbine-engine material. *MRS Bull.* **28**, 639–645 (2003).
- Ito, K., Kumagai, M., Hayashi, T. & Yamaguchi, M. Room temperature fracture toughness and high temperature strength of T₂/Mo_{ss} and (Mo, Nb)_{ss}/T₁/T₂ eutectic alloys in the Mo-Si-B system. *Scripta Mater.* **49**, 285–290 (2003).
- Yoshimi, K., Nakatani, S., Nomura, N. & Hanada, S. Thermal expansion, strength and oxidation resistance of Mo/Mo₅SiB₂ *in-situ* composites at elevated temperatures. *Intermetallics* **11**, 787–794 (2003).
- Hayashi, T., Ito, K., Ihara, K., Fujikura, M. & Yamaguchi, M. Creep of single crystalline and polycrystalline T₂ phase in the Mo-Si-B system. *Intermetallics* **12**, 699–704 (2004).
- Alur, A. P., Chollacoop, N. & Kumar, K. S. High-temperature compression behavior of Mo-Si-B alloys. *Acta Mater.* **52**, 5571–5587 (2004).
- Jain, P. & Kumar, K. S. Tensile creep of Mo-Si-B alloys. *Acta Mater.* **58**, 2124–2142 (2010).
- Miyamoto, S. *et al.* Phase equilibria, microstructure, and high-temperature strength of TiC-added Mo-Si-B alloy. *Metall. Mater. Trans. A* **45A**, 1112–1122 (2014).
- Choe, H., Chen, D., Schneibel, J. H. & Ritchie, R. O. Ambient to high temperature fracture toughness and fatigue-crack propagation behavior in a Mo-12Si-8.5B (at.%) intermetallic. *Intermetallics* **9**, 319–329 (2001).
- Schneibel, J. H., Ritchie, R. O., Kruzic, J. J. & Tortorelli, P. F. Optimization of Mo-Si-B intermetallic alloys. *Metall. Mater. Trans. A* **36A**, 525–531 (2005).
- Kruzic, J. J., Schneibel, J. H. & Ritchie, R. O. Ambient- to elevated-temperature fracture and fatigue properties of Mo-Si-B alloys: role of microstructure. *Metall. Mater. Trans. A* **36A**, 2393–2402 (2005).
- Lemberg, J. A. & Ritchie, R. O. Mo-Si-B alloys for ultrahigh-temperature structural applications. *Adv. Mater.* **24**, 3445–3480 (2012).
- Yoshimi, K. *et al.* High-temperature compressive properties of TiC-added Mo-Si-B alloys. *JOM* **66**, 1930–1938 (2014).
- Kamata, S. Y. *et al.* Ultrahigh-temperature tensile creep of TiC-reinforced Mo-Si-B-based alloy. *Sci. Rep.* **8**, 10487 (2018).
- Moriyama, T. *et al.* Room-temperature fracture toughness of MoSiBTiC alloys. *Intermetallics* **84**, 92–102 (2017).
- Nakamura, J., Kanekon, D. & Yoshimi, K. Characterization of Mo/Mo₂C interface in MoSiBTiC alloy. *Mater. Lett.* **180**, 340–343 (2016).
- Nowotny, H., Kieffer, R. & Benesovsky, F. Silicon borides of the transition metals vanadium, niobium, tantalum, molybdenum and tungsten. *Planseeberichte Fuer Pulvermetallurgie.* **5**, 86–93 (1957).
- Nunes, C. A., Sakidja, R., Dong, Z. & Perepezko, J. H. Liquidus projection for the Mo-rich portion of the Mo-Si-B ternary system. *Intermetallics* **8**, 327–337 (2000).
- Katrych, S. *et al.* Structural materials: metal-silicon-boron, On the melting behavior of Mo-Si-B alloys. *J. Alloy. Comp.* **347**, 94–100 (2002).
- Yang, Y. & Chang, Y. A. Thermodynamic modeling of the Mo-Si-B system. *Intermetallics* **13**, 121–128 (2005).
- Ha, S. *et al.* Experimental study of Mo_{ss}-T₂, Mo_{ss}-Mo₃Si-T₂, and Mo₃Si-T₂ eutectic reactions in Mo-rich Mo-Si-B. *J. Alloy. Comp.* **594**, 52–59 (2014).
- Kobatake, H., Fukuyama, H., Minato, I., Tsukada, T. & Awaji, S. Noncontact modulated laser calorimetry of liquid silicon in a static magnetic field. *J. Appl. Phys.* **104**, 054901 (2008).
- Tsukada, T., Fukuyama, H. & Kobatake, H. Determination of thermal conductivity and emissivity of electromagnetically levitated high-temperature droplet based on the periodic laser-heating method: Theory. *Int. J. Heat Mass Trans.* **50**, 3054–3061 (2007).
- Sugie, K. *et al.* Noncontact laser modulation calorimetry for high-purity liquid iron. *J. Appl. Phys.* **50**, 11RD04 (2011).
- Watanabe, M., Adachi, M. & Fukuyama, H. Densities of Fe-Ni melts and thermodynamic correlations. *J. Mater. Sci.* **51**, 3303–3310 (2016).
- Watanabe, M., Adachi, M. & Fukuyama, H. Normal spectral emissivity and heat capacity at constant pressure of Fe-Ni melts. *J. Mater. Sci.* **52**, 9850–9858 (2017).
- De Vos, J. C. Evaluation of The Quality of A Blackbody. *Physica* **XX**, 669–689 (1954).
- Preston-Thomas, H. The International Temperature Scale of 1990 (ITS-90). *Metrologia* **27**, 3–10 (1990).
- Yamada, Y., Sakate, H., Sakuma, F. & Ono, A. High-temperature fixed points in the range 1150 °C to 2500 °C using metal-carbon eutectics. *Metrologia* **38**, 213–219 (2001).
- Sasajima, N. *et al.* The dependence of the iron-carbon eutectic transition on thermal history and its implications for thermometry. *J. Alloy. Comp.* **452**, 61–66 (2008).
- Lü, P. & Wang, H. P. Effect of Undercooling and Cooling Rate on Peritectic Phase Crystallization Within Ni-Zr Alloy Melt. *Metall. Mater. Trans. B* **49B**, 499–508 (2018).
- Lü, P., Zhou, K. & Wang, H. P. Evidence for the transition from primary to peritectic phase growth during solidification of undercooled Ni-Zr alloy levitated by electromagnetic field. *Sci. Rep.* **6**, 39042 (2016).
- Eremenko, V. N. & Velikanova, T. Y. The Interaction of Molybdenum with Titanium Carbide. *Soviet Powder Metallurgy and Metal Ceramics, Translated from Poroshkovaya Metallurgiya, Kiev 2*, 347–352 (1963).
- Nunes, C. A., Sakidja, R. & Perepezko, J. H. Phase Stability in High Temperature Mo-RICH Mo-B-Si Alloys, *Structural Intermetallics 1997*, Edited by Nathal, M. V. *et al.*, The Minerals, Metals & Materials Society, 1997, pp. 831–839.

Acknowledgements

This work was supported by the Advanced Low Carbon Technology Research and Development Program (ALCA) of the Japan Science and Technology Agency (JST) (No. JPMJAL1303). The authors thank the National Institute of Advanced Industrial Science and Technology (AIST) for advice on designing a crucible having a blackbody cavity.

Author contributions

M.O., K.Y. and H.F. designed this research. R.S. and H.N. carried out the experiments and analysed the data. H.F., M.O. and K.Y. wrote the main manuscript text and R.S. and H.N. prepared figures. All authors contributed to discussion of the results and reviewed the manuscript.

Competing interests

The authors declare no competing interests.

Additional information

Supplementary information is available for this paper at <https://doi.org/10.1038/s41598-019-50945-z>.

Correspondence and requests for materials should be addressed to H.F.

Reprints and permissions information is available at www.nature.com/reprints.

Publisher's note Springer Nature remains neutral with regard to jurisdictional claims in published maps and institutional affiliations.



Open Access This article is licensed under a Creative Commons Attribution 4.0 International License, which permits use, sharing, adaptation, distribution and reproduction in any medium or format, as long as you give appropriate credit to the original author(s) and the source, provide a link to the Creative Commons license, and indicate if changes were made. The images or other third party material in this article are included in the article's Creative Commons license, unless indicated otherwise in a credit line to the material. If material is not included in the article's Creative Commons license and your intended use is not permitted by statutory regulation or exceeds the permitted use, you will need to obtain permission directly from the copyright holder. To view a copy of this license, visit <http://creativecommons.org/licenses/by/4.0/>.

© The Author(s) 2019